

# Improved Capacity Retention for a Disordered Rocksalt Cathode via Solvate Ionic Liquid Electrolytes

Lennart Wichmann,<sup>[a, b]</sup> Jan-Paul Brinkmann,<sup>[b]</sup> Mingzeng Luo,<sup>[c]</sup> Yong Yang,<sup>[c]</sup> Martin Winter,<sup>[a, b]</sup> Richard Schmuck,<sup>[a]</sup> Tobias Placke,\*<sup>[a]</sup> and Aurora Gomez-Martin\*<sup>[a]</sup>

Lithium-rich disordered rocksalts (DRX) are a promising class of cathode materials for high-energy lithium ion batteries (LIBs) and lithium metal batteries (LMBs) due to the high initial specific capacities ( $> 200 \text{ mAh g}^{-1}$ ) as well as flexible chemical composition. However, challenges concerning severe capacity fade and voltage decay upon cycling at high cut-off voltages are still to be overcome. Moreover, state-of-the-art carbonate-based electrolytes can be decomposed by reactive oxygen species released by DRX materials during cycling. In this work,

the electrochemical performance of  $\text{Li}_{1.25}\text{Fe}_{0.5}\text{Nb}_{0.25}\text{O}_2$  (LFNO) || Li LMB and LFNO || graphite LIB cells is compared for a conventional, carbonate-based electrolyte and the solvate ionic liquid (SIL)  $[\text{Li}(\text{G3})][\text{TFSI}]$  (G3: triethyleneglycoldimethylether). Cycle life is notably improved by the chemically more stable ionic liquid electrolyte, as the anionic redox activity of LFNO is prolonged compared to the carbonate-based cells. This work represents an important step toward an improved cycle life of DRX cathodes.

## Introduction

Due to their high energy efficiency and energy density, lithium-ion batteries (LIBs) currently dominate the battery market for portable electronic devices, stationary energy storage as well as hybrid, plug-in or full electric vehicles.<sup>[1]</sup> However, for their widespread application it is necessary to further improve their energy density while also decreasing costs along the whole battery value circle.<sup>[2–4]</sup> As of now, layered lithium nickel cobalt manganese oxides  $\text{Li}[\text{Ni}_x\text{Mn}_y\text{Co}_z]\text{O}_2$  ( $x+y+z=1$ ; further abbreviated as NMC) are the state-of-the-art (SOTA) high capacity positive electrode (cathode) materials for LIBs due to their high technological maturity.<sup>[5]</sup> They are also candidates for future

rechargeable lithium metal batteries (LMBs).<sup>[6]</sup> Compared to SOTA graphite-based negative electrode (anode) materials, NMC-based cathodes only offer a limited specific energy ( $\text{Wh kg}^{-1}$ ) due to their comparatively low specific capacities ( $\text{Ah kg}^{-1}$ ) due to limited Li utilization. Furthermore, NMC relies on scarce transition metals such as nickel and cobalt, which raise concerns regarding future supply reliability and costs as well as environmental and ethical implications.<sup>[2]</sup> Therefore, the exploration of novel positive electrode materials offering higher specific capacities is of high interest for the battery community.<sup>[4, 7]</sup>

Lithium transition metal oxides adopting a disordered rock salt (DRX) crystal structure have emerged as a promising alternative to SOTA NMC-type cathode materials over the last few years, since they display higher initial discharge capacities ( $> 200 \text{ mAh g}^{-1}$ ) and a broad compositional range, which allows using several redox chemistries with more abundant, low-cost and less toxic transition metals compared to nickel and cobalt (e.g., Mn,<sup>[8–10]</sup> V<sup>[8]</sup> or Fe<sup>[11,12]</sup>). Instead of lithium diffusion inside the lithium layers, as found in conventional layered oxides, the lithium diffusion in these DRX materials takes place along a percolation network of migration channels without adjacent transition metal cations (0 TM channels), which is enabled by a certain amount of lithium excess ( $x > 0.09$  in  $\text{Li}_{1+x}\text{TM}_{1-x}\text{O}_2$ ).<sup>[13]</sup> The increased lithium content also alternates the local environment of the oxides, which makes the O2p orbital accessible for oxidation at high potentials ( $\geq 4 \text{ V vs. Li}|\text{Li}^+$ ).<sup>[14]</sup> Therefore, DRX-type cathodes, similarly to Li-rich layered oxides, have been reported to display anionic redox activity in addition to common cationic redox reactions of the respective transition metals.<sup>[15,16]</sup> While the reversible proportion of oxygen redox contributes to the high discharge capacity of DRX materials and is considered beneficial, irreversible oxygen redox inevitably results in the release of gaseous oxygen and structural transitions due to lattice-vacancies left behind. Thus, DRX

[a] L. Wichmann, Prof. Dr. M. Winter, Dr. R. Schmuck, Dr. T. Placke, Dr. A. Gomez-Martin

University of Münster

MEET Battery Research Center,

Institute of Physical Chemistry

Corrensstr. 46, 48149

Münster, Germany

E-mail: tobias.placke@uni-muenster.de

agomezma@uni-muenster.de

[b] L. Wichmann, J.-P. Brinkmann, Prof. Dr. M. Winter

Helmholtz-Institute Münster

IEK-12, Forschungszentrum Jülich GmbH

Corrensstr. 46, 48149

Münster, Germany

[c] M. Luo, Prof. Dr. Y. Yang

State Key Laboratory of Physical Chemistry of Solid Surfaces

Department of Chemistry,

College of Chemistry and Chemical Engineering

Xiamen University

361005 Xiamen, China

 Supporting information for this article is available on the WWW under <https://doi.org/10.1002/batt.202200075>

 © 2022 The Authors. *Batteries & Supercaps* published by Wiley-VCH GmbH. This is an open access article under the terms of the Creative Commons Attribution License, which permits use, distribution and reproduction in any medium, provided the original work is properly cited.

cathodes exhibit rapid capacity fade on cycling and face several challenges, which still hinder their practical application.<sup>[16,17]</sup>

As pointed out by Assat and Tarascon, the amount of anionic redox activity and oxygen release can be influenced by selection of the metal species, since the energetic level of its d-orbitals relative to the non-bonding oxygen orbitals correlates with the amount of anionic redox activity and its reversibility. However, to obtain TM d-states low enough in energy, one needs to select elements further down the periodic table, e.g., Ir instead of Mn, which significantly increases material costs.<sup>[18]</sup> Alternatively, anionic-substitution by fluorine allows to increase the content of the redox-active TM and can thereby lower or even prevent anionic redox.<sup>[19]</sup> On the one hand, this approach successfully alleviates the issues associated with oxygen release, but on the other hand, it omits the opportunity to utilize the reversible proportion of oxygen redox and thereby reduces the attainable specific discharge capacity. Therefore, further strategies to mitigate the negative impact of released oxygen are necessary for the practical implementation of DRX cathode materials.

In the context of oxygen released from Li-rich layered oxides during delithiation of the cathode (i.e., charge), previous reports gave evidence for the electrochemical reduction of oxygen molecules below 3 V during the following discharge (= lithiation) step. This one electron reaction is thought to result in the formation of superoxide species, which decompose conventional electrolytes based on organic carbonates.<sup>[20]</sup> As the charge and discharge capacities of DRX positive electrodes rely to a large extent on anionic redox activity, the decomposition of SOTA carbonate-based electrolytes due to oxygen species released by the irreversible proportion of anionic redox can be considered as one of many factors contributing to the drastic capacity fade exhibited by DRX cathodes.<sup>[10,13,14,16,17]</sup> Although the abrupt capacity fade shown by various DRX cathodes is caused by an interplay of several degradation phenomena, this study focuses on alleviating electrolyte decomposition and its detrimental impact on cycle life for DRX-based cells.

To avoid continuous electrolyte decomposition as a result of oxygen release during cell operation, the use of an (electro)chemically more stable electrolyte is necessary. Despite their higher costs as well as worse electrochemical performance at temperatures lower than 40 °C, room temperature ionic liquids (RTILs) are considered suitable candidates, as their ionic nature results in a low chemical reactivity and high oxidative stability, which qualify them as electrolytes for high-voltage applications.<sup>[21]</sup> Furthermore, their application in Li||air batteries, where LiO<sub>2</sub> is formed as an intermediate, has already proven their low reactivity towards reduced O<sub>2</sub> species.<sup>[22]</sup> However, graphite exfoliation due to RTIL cation co-intercalation (e.g., Pyr<sub>14</sub>) as well as low ionic conductivities below or at room temperature limit their practical application in standard LIBs.<sup>[23]</sup> In contrast, solvate ionic liquids (SILs), a sub-group of RTILs that are synthesized by combining a Li salt and a high donor number solvent (e.g., triethyleneglycoldimethyl ether) to form the cationic (Li<sup>+</sup> and solvent) and anionic (Li salt anion) species of the ionic liquid, overcome the issue of cation co-

intercalation at the graphite anode and hold promise for application in LIB cells. The unique design of the cationic species within the ionic liquid requires high concentrations of the respective lithium salt, which consequently results in high viscosity and low ionic conductivity, but also enables stable operation with a graphite negative electrode, as no free solvent molecules are present that could co-intercalate into graphite.<sup>[24–26]</sup> Furthermore, the challenge of comparatively low ionic conductivities can be alleviated by the dilution with a co-solvent (e.g., with a hydrofluoroether (HFE)), while the electrolyte remains compatible with graphite as shown by Moon et al. utilizing the diluted and undiluted SILs [Li(G3)<sub>1</sub>][TFSI] (with G3 = triethyleneglycoldimethyl ether) in LiCoO<sub>2</sub> || graphite LIB cells.<sup>[25]</sup> Additionally, the application of these SILs in Li-air batteries gives evidence of a high (electro)chemical stability towards reactive oxygen species.<sup>[27]</sup> These electrolytes can thus be a suitable option to alleviate one of the factors contributing to the typical capacity fade shown by DRX cathode materials in carbonate-based electrolytes.

Therefore, a SIL electrolyte, i.e., [Li(G3)][TFSI], is herein investigated as an alternative electrolyte for DRX-based LIB cells. The DRX material Li<sub>1.25</sub>Fe<sub>0.5</sub>Nb<sub>0.25</sub>O<sub>2</sub> (LFNO), which is based on Fe as an environmentally friendly TM and provides high initial discharge capacity, is selected as the active material representing the oxygen redox-based cathodes. Furthermore, its redox mechanism has been thoroughly investigated in a previous report, which revealed high proportions of anionic redox.<sup>[11]</sup> As in this work the impact of anionic redox on electrolyte decomposition is compared for a carbonate-based reference electrolyte and solvate ionic liquids, LFNO with comparatively low TM and high anionic redox capacity can be considered as an ideal positive electrode material. Therefore, the electrochemical performance of LFNO || Li LMB cells and LFNO || graphite LIB cells using undiluted and diluted SILs G3: LiTFSI and G3:LiTFSI:HFE will be evaluated relatively to the performance with a SOTA carbonate-based liquid electrolyte (1 M LiPF<sub>6</sub> in ethylene carbonate:ethyl methyl carbonate (EC: EMC) 3:7 by wt.%). Electrochemical impedance spectroscopy (EIS), attenuated total reflectance Fourier-transformed infra-red spectroscopy (ATR-FTIR) and scanning electron microscopy (SEM) are used to investigate the properties of the electrodes and interphases formed by the different electrolytes at the cathode|electrolyte interfaces, thereby causing notable differences in the capacity retention and cycle life.

## Results and Discussion

### Dissolution of the Al current collector

Since the Al current collector is prone to oxidation at high potentials vs. Li|Li<sup>+</sup>, Al dissolution in high-voltage batteries can cause severe capacity fade due to contact loss with the active material.<sup>[28,29]</sup> Organic carbonate-based electrolytes using LiPF<sub>6</sub> as their electrolyte salt are known to form an effective, fluoride-containing passivation layer that prevents Al dissolution at high operating potentials.<sup>[28,30]</sup> In contrast, LiTFSI as electrolyte salt

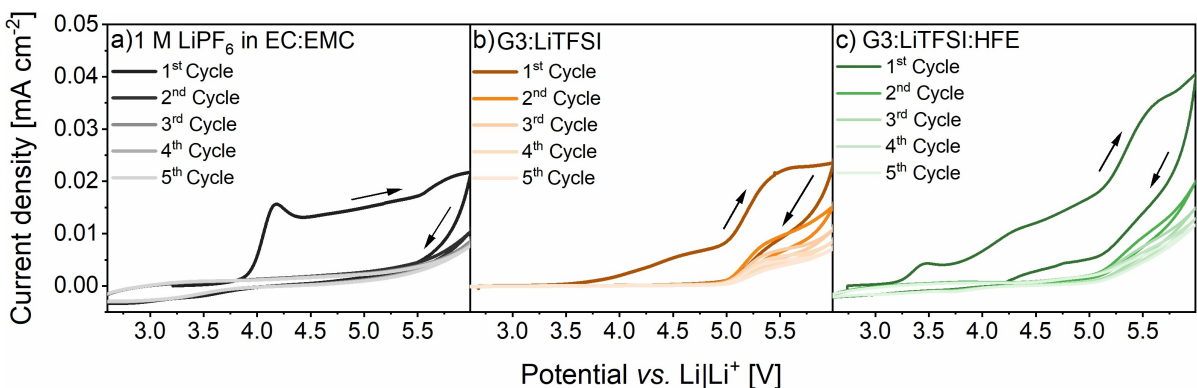


**Figure 1.** Cyclic voltammograms of  $\text{Al} \parallel \text{Li}$  LMB cells for the first five cycles using Li metal as counter electrode (CE) and reference electrode (RE) and Al foil as the working electrode (WE) in: a) Reference electrolyte, b) G3:LiTFSI and c) G3:LiTFSI:HFE. Measurements have been conducted in a potential range from 2.5 to 6.0 V vs.  $\text{Li} \parallel \text{Li}^+$  using a scan rate of  $0.1 \text{ mVs}^{-1}$  at  $20^\circ\text{C}$ .

does not passivate the current collector effectively and can dissolve it to form  $\text{Al}(\text{TFSI})_y$  complexes.<sup>[28,31]</sup> To investigate whether SILs based on LiTFSI can serve as a suitable electrolyte for positive DRX electrodes with an Al current collector, cyclovoltammetry (CV, Figure 1) as well as chronocoulometry (CC, Figure 2) measurements using freshly-etched Al foil were conducted.

During the CV measurements, the electrochemical force, which results from the polarization in anodic direction, leads to the oxidation of Al foil and the formation of  $\text{Al}^{3+}$  species. Since electron release of oxidation processes induces charge transfer and a current flow, the current density is a measure of Al dissolution as well as other oxidative processes.<sup>[32]</sup> As can be seen in Figure 1, the highest current density is observed in the 1<sup>st</sup> cycle for all electrolytes, whereas the current density in the diluted SIL (G3:LiTFSI:HFE) is the highest. With ongoing cycles, the current density decreases steadily for all electrolytes. Furthermore, the anodic scan exhibits higher current densities than the cathodic scan in each cycle. Both observations indicate the decrease of Al oxidation throughout cycling. Previous investigations on SILs have shown, that the disappearance of Al dissolution in these electrolytes can be attributed to their high salt concentration and therefore low availability of uncoordinated solvent molecules, which hinders the formation of  $\text{Al}(\text{TFSI})_y$  complexes and thus dissolution of  $\text{Al}^{3+}$ .<sup>[24,25]</sup> To probe the Al dissolution under harsher operating conditions, CC measurements at 5.0 V vs.  $\text{Li} \parallel \text{Li}^+$  were conducted at  $20^\circ\text{C}$  for 48 h. The cumulative charge values (Figure 2) give an indication of occurring parasitic reactions, mainly originating from oxidative decomposition of electrolyte components and Al dissolution.<sup>[28]</sup>

In agreement with the CV measurements, it can be observed that the degree of Al dissolution is in the same magnitude order for the reference and SIL electrolytes. Nevertheless, the cumulative charge in the SILs is higher and steadily increases over time, whereas the cumulative charge for the  $\text{LiPF}_6$ /organic carbonate-based electrolyte levels off after a steep increase within the first 3 h. This can be attributed to the different mechanisms that alleviate Al dissolution for each electrolyte, which are the passivation by  $\text{LiPF}_6$  decomposition

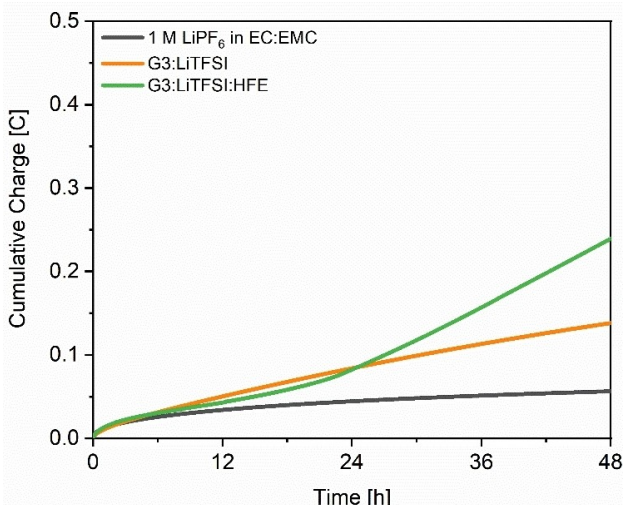


**Figure 2.** Chronocoulometry (CC) measurements for 48 h at 5.0 V vs.  $\text{Li} \parallel \text{Li}^+$  using  $\text{Al} \parallel \text{Li}$  LMB cells (WE: Al; CE and RE: Li metal) with the reference electrolyte, G3:LiTFSI and G3:LiTFSI:HFE at  $20^\circ\text{C}$ .

for the reference electrolyte and the insolubility of  $\text{Al}(\text{TFSI})_y$  complexes for the SILs.<sup>[24,25,28]</sup> Although  $\text{Al}(\text{TFSI})_y$  complexes have been reported to be hardly soluble in the diluted SIL G3:LiTFSI:HFE, it still exhibits a higher cumulative charge than the undiluted SIL.<sup>[25]</sup> Possible explanations include the dissolution of these Al complexes by the diluent itself or the coordination of a small amount of  $\text{Li}^+$  by the diluent HFE, which would result in free glyme molecules able to dissolve the  $\text{Al}(\text{TFSI})_y$  species. Alternatively, the additional charge relative to the undiluted SIL as the electrolyte could be due to decomposition reactions of the HFE at these high potentials. However, as the absolute current density in both SILs is similar to the reference system and notably lower than what was observed for cases of severe Al dissolution, its impact on the electrochemical performance during charge/discharge operation can be considered as negligible.<sup>[28]</sup>

### Electrochemical performance of LFNO || Li LMB and LFNO || graphite LIB cells

Without any notable Al dissolution observed, the undiluted and diluted SILs can be directly compared to the organic carbonate-based SOTA electrolyte in LFNO || Li LMB and LFNO || graphite LIB cells. Cells were charged/discharged at 0.1 C (30 mAh g<sup>-1</sup>) for 100 cycles in a voltage range of 1.5–4.6 V for LMB cells and 0.5–4.6 V for LIB cells. At an elevated temperature of 60 °C the cut-off voltage for both cell setups was lowered to 4.5 V, as electrolyte decomposition was observed at 4.6 V. The Coulombic efficiencies ( $C_{\text{Eff}}$ , Figure 3a–c) and discharge capacities ( $Q_{\text{Dis}}$ , Figure 3d–f) for the LMB cells assembled with the SILs and the reference electrolyte at 20, 40 and 60 °C are shown in Figure 3.

Since the viscosity of the SILs is temperature-dependent and directly impacts their ionic conductivity (Figure S1, Supporting Information), the overall cycling performance displayed

by the LFNO || Li LMB cells with the diluted and undiluted SIL differs the most at 20 °C. Due to the higher electrolyte resistance of the more viscous, undiluted electrolyte G3:LiTFSI, the specific discharge capacities at 20 °C (Figure 3a) are ≈40 mAh g<sup>-1</sup> lower than for cells assembled with the diluted SIL G3:LiTFSI:HFE. At 40 °C and 60 °C, the viscosity of the electrolyte becomes less of a drawback and the cells using the diluted and undiluted SILs display similar initial specific discharge capacities as well as capacity retention.

Compared to the reference carbonate-based electrolyte system, the cells with the SILs as electrolyte exhibit an improved capacity retention over cycling at each temperature. Cells retain 60% (reference electrolyte), 81% (G3:LiTFSI) and 75% (G3:LiTFSI:HFE) of the 1<sup>st</sup> cycle discharge capacity after 100 cycles at 20 °C. The enhanced cycling stability of the cells using the SILs as electrolyte is particularly pronounced at elevated temperatures (40 and 60 °C), where a complete

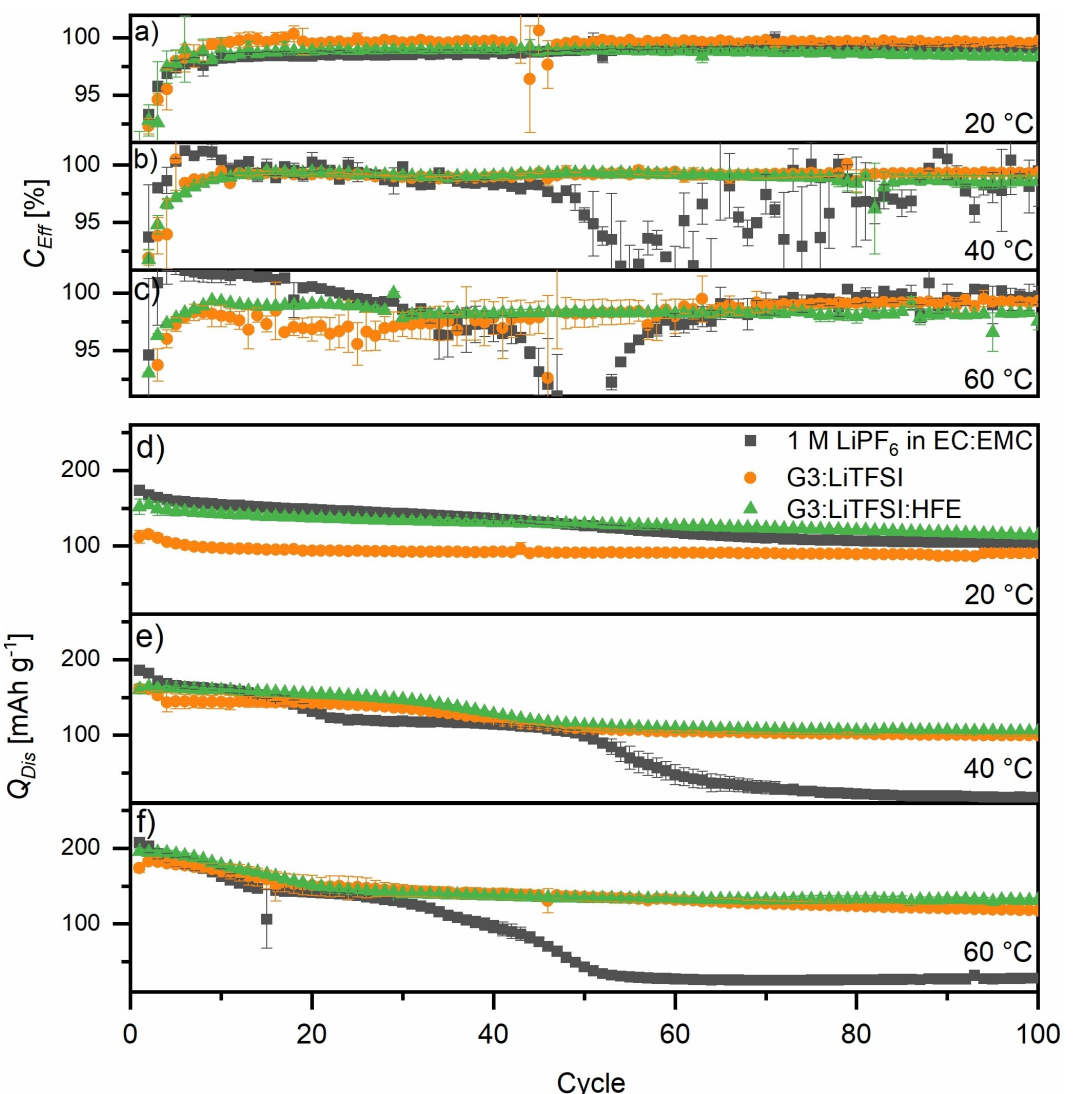


**Figure 3.** Coulombic efficiencies ( $C_{\text{Eff}}$ ) and discharge capacities ( $Q_{\text{Dis}}$ ) of LFNO || Li LMB cells using 1 M LiPF<sub>6</sub> in EC:EMC, G3:LiTFSI and G3:LiTFSI:HFE as the electrolyte at a), d) 20 °C, b and e) 40 °C, c and f) 60 °C, respectively. Voltage range: 1.5–4.6 V at 20 °C and 40 °C; 1.5–4.5 V at 60 °C. Charge/discharge current: 0.1 C (30 mAh g<sup>-1</sup>).

depletion of the discharge capacity within 100 cycles occurs for cells using the reference electrolyte. This accelerated capacity decay of the reference cells upon cycling can be divided into two separate regions, of which the latter one coincides with a drastically reduced  $C_{\text{Eff}}$  ( $\approx 40^{\text{th}}$  cycle). For the cells using the SILs on the other hand, only one sloping region of capacity decay and relatively stable  $C_{\text{Eff}}$  can be observed. This trend can also be confirmed in the accumulated Coulombic inefficiency (ACIE, Figure 4), which is a measure of parasitic electrochemical reactions throughout cycling.<sup>[33]</sup> At elevated temperatures, the cells assembled with the reference electrolyte initially exhibit a decrease in ACIE due to  $C_{\text{Eff}} > 100\%$  (Figure 4b and c), indicating extra discharge capacity. This additional discharge

capacity could originate from electrochemical decomposition of solid electrolyte interphase (SEI)/cathode electrolyte interphase (CEI) products that formed by chemical reactions between the electrolyte and the negative or positive electrode and thus did not consume current upon charge. More likely, the extra discharge capacity could also originate from lithiation of the positive electrode with excess lithium from the negative lithium metal electrode. These additional lithium ions could either migrate into tetrahedral sites, octahedral vacancies that were kinetically hindered in earlier cycles (e.g., shown for layered oxides) or TM vacancies that result from the oxygen loss and the associated cation densification to maintain electro-neutrality at the microscopic scale.<sup>[34]</sup> These observations will be the subject of further studies. However, it is important to note that  $C_{\text{Eff}} > 100\%$  lower the ACIE, giving the impression of less irreversible reactions for the SOTA electrolyte at elevated temperatures (see Figure 4c). Adjusting the ACIE for the  $C_{\text{Eff}} > 100\%$  region results in similar ACIEs after 100 cycles at 60 °C regardless of the electrolyte.

To investigate whether the improved capacity retention and reversibility is transferable from the LMB to the LIB cell setup without an unlimited reservoir of active lithium ions (i.e., without a Li metal negative electrode), LFNO || graphite LIB cells were also assembled with both SILs as well as with the carbonate-based electrolyte. Figure 5 shows the rate capability of the different electrolyte formulations at 40 °C at increasing charge and discharge C-rates (from 0.1 C to 2 C) in a cell voltage range of 0.5–4.6 V.

The drawbacks associated with the lower ionic conductivity of the undiluted electrolyte G3:LiTFSI, which already became evident in the LFNO || Li LMB cells at 20 °C (Figure 3a), are also noticeable in the C-rate investigations at 40 °C. While the LIB cells using G3:LiTFSI as the electrolyte show improved  $C_{\text{Eff}}$  and capacity retention compared to the reference electrolyte system at a C-rate of 0.1 C (30 mA g<sup>-1</sup>), they suffer from poor ionic transport within the electrolyte at higher currents ( $\geq 0.5$  C), leading to notably reduced discharge capacities. The dilution of the SIL by addition of HFE results in a notable improvement in ionic conductivity (Figure S1), and thus in rate capability. Discharge capacities and  $C_{\text{Eff}}$  values higher than for the reference system can still be maintained after doubling the rate to 0.2 C (60 mA g<sup>-1</sup>) and a similar performance compared to the reference system can be maintained at 0.5 C. However, with further increase of the current ( $\geq 1$  C) the drawback of lower ionic conductivity compared to the reference electrolyte (Figure S1) limits the improvements provided by the SILs.

The long-term cycling performance of LFNO || graphite cells using the different electrolyte formulations was also investigated at 20, 40 and 60 °C. Note again that at 60 °C the upper cut-off voltage was lowered to 4.5 V to avoid electrolyte decomposition. The comparison of the Coulombic efficiencies ( $C_{\text{Eff}}$ , Figure 6a–c) and discharge capacities ( $Q_{\text{Dis}}$ , Figure 6d–f) in the different electrolytes within 100 cycles at 20, 40 and 60 °C are shown in Figure 6. The corresponding cell voltage profiles for different cycle numbers can be found in Figures S2–S4.

Although the limitations of LIB cells using either SIL at higher currents became already evident from the C-rate

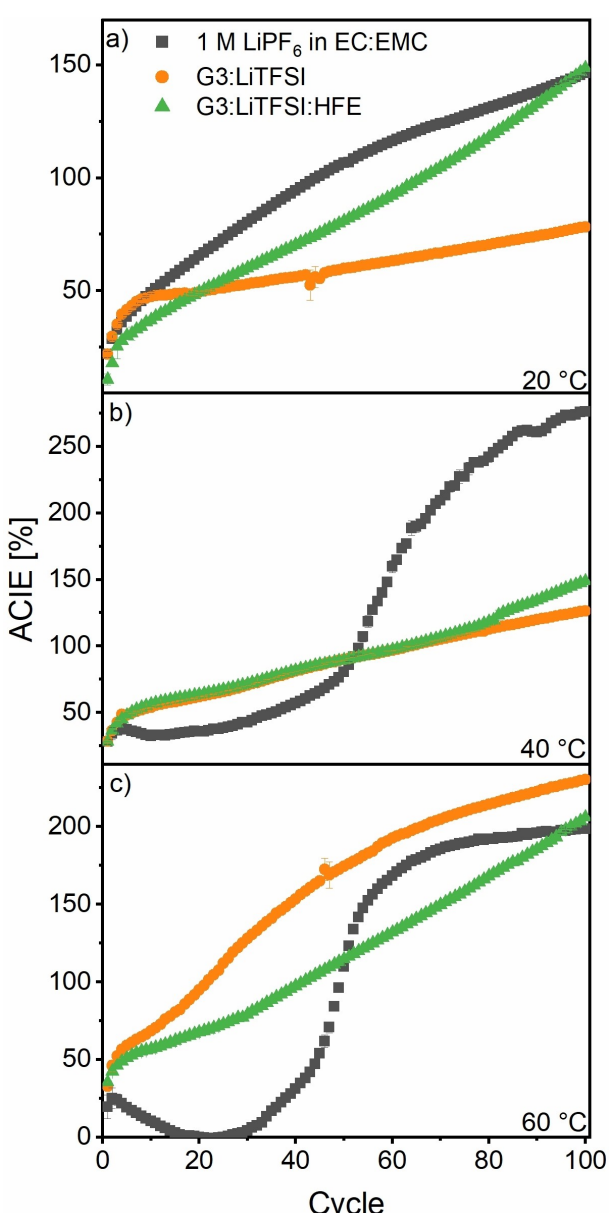


**Figure 4.** Accumulated Coulombic inefficiencies (ACIE) of LFNO || Li LMB cells using the reference electrolyte, G3:LiTFSI and G3:LiTFSI:HFE as the electrolyte at a) 20 °C, b) 40 °C and c) 60 °C. Voltage range: 1.5–4.6 V at 20 °C and 40 °C; 1.5–4.5 V at 60 °C, charge/discharge current: 0.1 C (30 mA g<sup>-1</sup>).

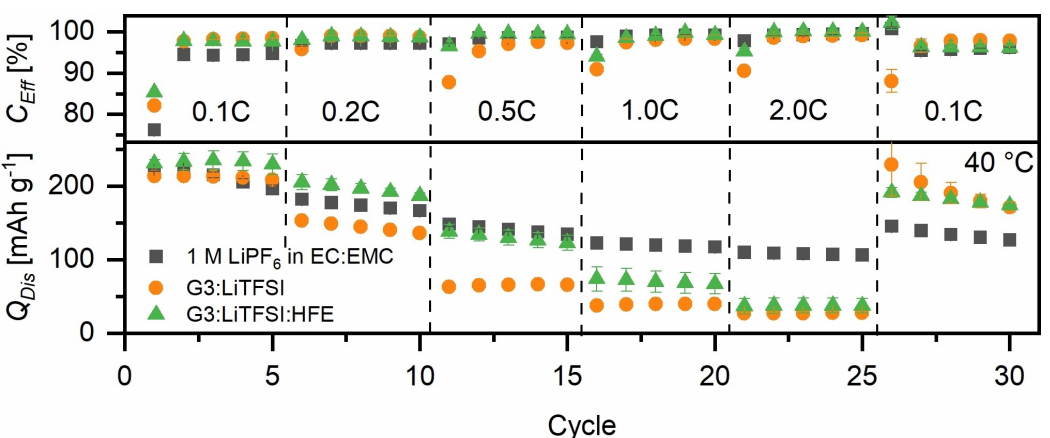


**Figure 5.** Rate capability experiments at different charge/discharge rates from 0.1 C to 2 C (1 C = 300 mA g $^{-1}$ ) for LFNO || graphite cells (LIB cell setup, control of cell voltage) at 40 °C assembled with the reference electrolyte, G3:LiTFSI and G3:LiTFSI:HFE. Cell voltage range: 1.5–4.6 V.

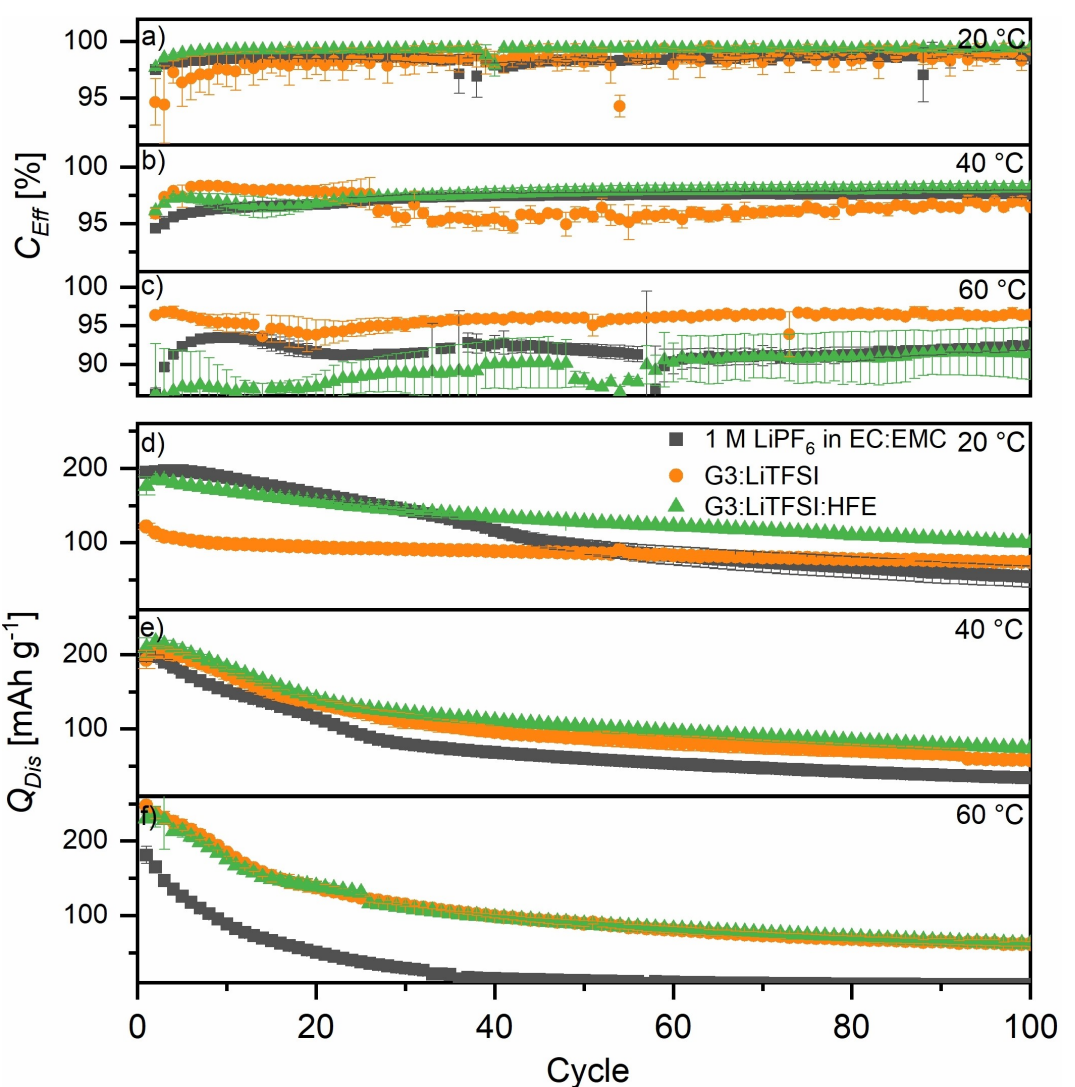


**Figure 6.** Discharge capacities ( $Q_{\text{Dis}}$ ) and Coulombic efficiencies ( $C_{\text{Eff}}$ ) of LFNO || graphite cells (LIB cell setup, control of cell voltage) assembled with the reference electrolyte, G3:LiTFSI and G3:LiTFSI:HFE at a and d) 20 °C, b and e) 40 °C, c and f) 60 °C. Cell voltage range: 0.5–4.6 V at 20 and 40 °C; 0.5–4.5 V at 60 °C, charge/discharge current: 0.1 C (30 mA g $^{-1}$ ).

investigation, improved  $C_{\text{eff}}$  as well as discharge capacities compared to the reference system could be observed within 5 cycles at 40 °C and a low specific current of 30 mAh g<sup>-1</sup> (0.1 C). Consequently, LIB cells assembled with both SILs exhibit a higher discharge capacity and capacity retention after 100 cycles at 0.1 C at 40 and 60 °C (Figure 6b and c), analogous to the performance of LMB cells. Additionally, improved capacity retention can also be observed at 20 °C, although the performance in SIL electrolytes are most limited by their high viscosity at this temperature. However, the improved  $C_{\text{eff}}$  observed in LMB cells is not directly transferable to the LIB cell setup. The  $C_{\text{eff}}$  for cells using G3:LiTFSI at 40 °C and G3:LiTFSI:HFE at 60 °C exhibit an unstable behavior and fluctuations, which are also reflected in the ACIE evolution (Figure 7b and c). As higher and more stable  $C_{\text{eff}}$  have been observed with a lithium metal negative electrode, these fluctuations can be ascribed to irreversible reactions occurring at the graphite|SIL interface.

Nevertheless, the LIB cells assembled with the diluted SIL (G3:LiTFSI:HFE) show improved reversibility (ACIE) at 20 and 40 °C and outperform the reference system in terms of capacity retention at every temperature. Only at 60 °C the ACIE of cells assembled with G3:LiTFSI:HFE is less stable compared to the carbonate-based electrolyte, which is not of much significance as the discharge capacity of the reference system is already degraded to < 20 mAh g<sup>-1</sup> after 35 cycles. Generally speaking, increased initial discharge capacities, but severely deteriorated cycling stability can be observed with increasing temperature regardless of the electrolyte formulation, as previously reported for DRX positive electrodes.<sup>[12,35]</sup>

The cause for improved cycle life of LFNO-based LIB and LMB cells using SILs as electrolyte becomes evident from the differential capacity ( $dQ/dV$ ) vs. voltage plots from LFNO || graphite cells depicted in Figure 8. As previously reported by Luo et al., oxygen oxidation in LFNO (represented by the cathodic peak labelled as Ox<sub>2</sub>), which coincides with the oxidation of Fe<sup>3+</sup> to Fe<sup>4+</sup> and the subsequent reduction via a reductive coupling mechanism, occurs at cell voltages above 4 V.<sup>[11]</sup>

For cells assembled using the reference electrolyte, the cathodic peak associated with this process shifts towards higher cell voltages throughout cycling, which indicates the occurrence of a steadily increasing overpotential. This overpotential shifts the anionic oxidation beyond the upper cut-off voltage, which causes the depletion of the anionic redox activity. Fittingly, the depletion of the anionic redox activity coincides with a reduced slope of capacity fade, e.g., little to no Ox<sub>2</sub> peak in the  $dQ/dV$  vs. voltage plot of the 25<sup>th</sup> cycle in the reference electrolyte at 40 °C (Figure 8b, anionic redox almost depleted) and a reduced slope for the decline of discharge capacity after ≈25 cycles in Figure 5(e). Analogously, the change in slope of capacity fade for the reference system at 20 °C after ≈50 cycles (Figure 6d) can be correlated with the depletion of anionic redox activity (Figure 8a).

For the cells using SILs as electrolyte, the overpotential for the oxygen oxidation increases at a lower rate. Thus, the contribution of anionic redox to the overall capacity is

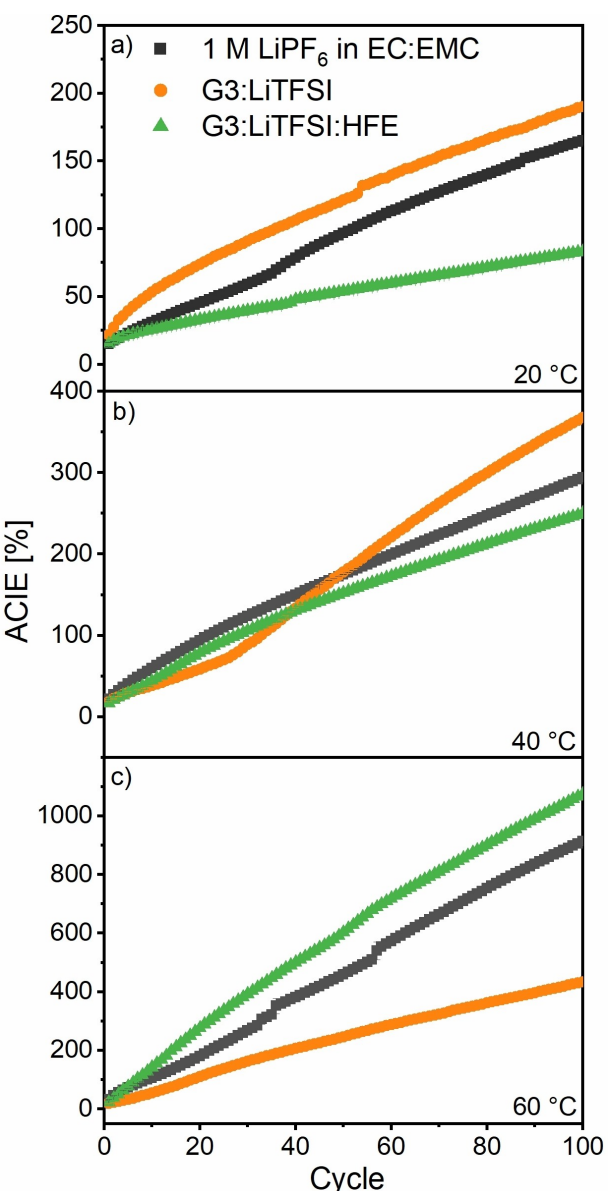


**Figure 7.** Accumulated Coulombic inefficiencies (ACIE) of LFNO || graphite cells (LIB-cell setup, control of cell voltage) assembled with the reference electrolyte, G3:LiTFSI and G3:LiTFSI:HFE at a) 20 °C, b) 40 °C and c) 60 °C. Cell voltage range: 0.5–4.6 V at 20 and 40 °C; 0.5–4.5 V at 60 °C, charge/discharge current: 0.1 C (30 mAh g<sup>-1</sup>).

extended, which benefits capacity retention. Comparing anionic oxidation for the same electrolyte at different temperatures (e.g., Figure 8a–c) further reveals that an increasing temperature accelerates the loss of anionic redox activity in all electrolytes. Still, the oxygen oxidation depletes the earliest in cells using the carbonate-based electrolyte regardless of the temperature. Besides the depletion of anionic redox activity, a further capacity fade mechanism can be observed from the  $dQ/dV$  vs. voltage plots at 40 and 60 °C. The cathodic and anodic peaks corresponding to the oxidation and reduction of the redox active transition metal Fe (labelled as Ox<sub>1</sub> and Red<sub>1</sub>) also exhibit an increasing overpotential and a reduced intensity throughout cycling. Similar to the anionic redox activity,

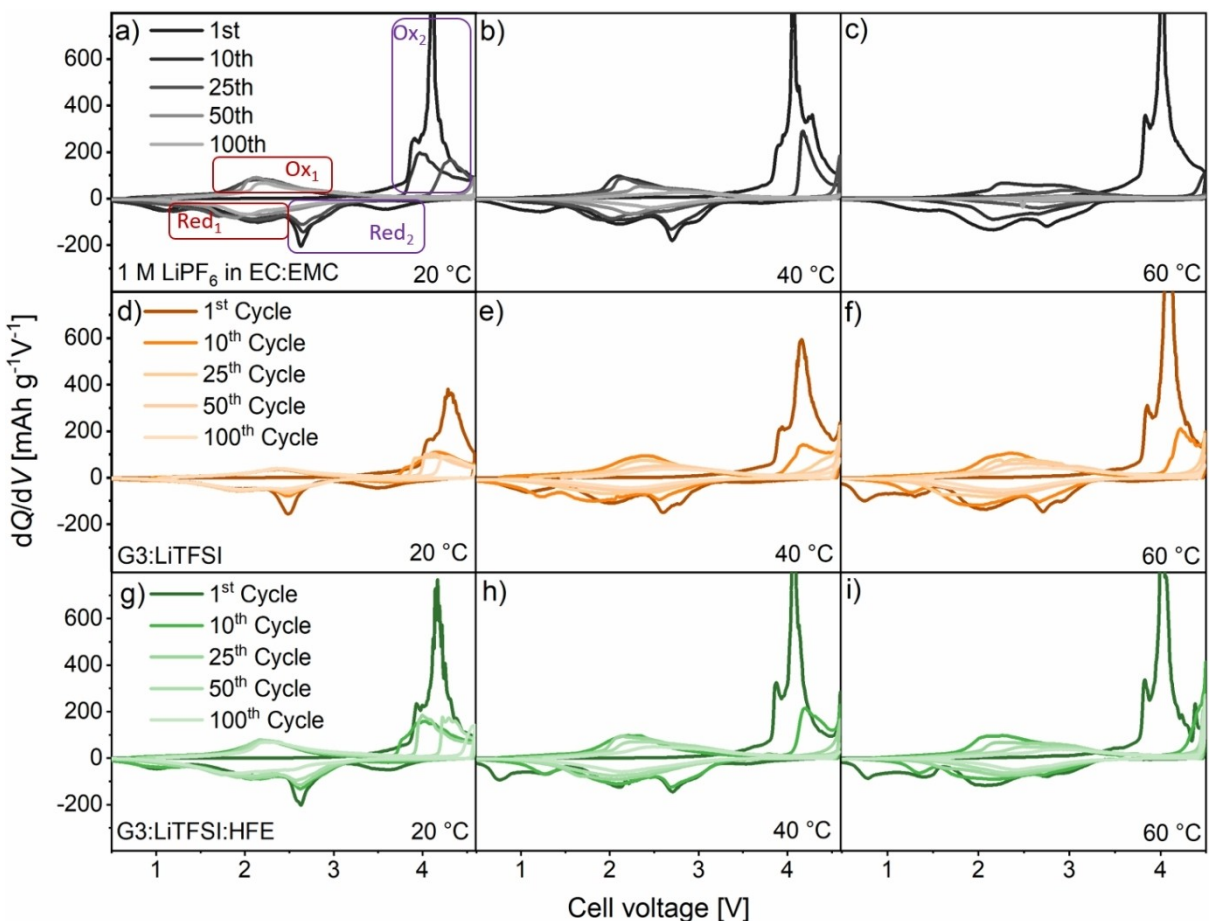


**Figure 8.** Differential capacity vs. voltage plots for the 1<sup>st</sup>, 10<sup>th</sup>, 25<sup>th</sup>, 50<sup>th</sup> and 100<sup>th</sup> cycle of LFNO || graphite cells (LIB cell setup, control of cell voltage) assembled with a–c) the reference electrolyte, d–f) G3:LiTFSI and g–i) G3:LiTFSI:HFE at 20, 40 and 60 °C. The related redox processes for the TM and dominantly anionic redox (Ox<sub>1</sub>/Red<sub>1</sub> and Ox<sub>2</sub>/Red<sub>2</sub>) are marked in the dQ/dV vs. voltage plot at 20 °C (a) according to Reference [11]. Cell voltage range: 0.5–4.6 V at 20 and 40 °C; 0.5–4.5 V at 60 °C, charge/discharge current: 0.1 C (30 mA g<sup>-1</sup>).

deterioration of TM redox is alleviated for the cells using the SILs, as the overpotential increases at a lower rate and higher intensities can be maintained.

The steadily increasing overpotentials for the TM and anionic redox activities in the reference electrolyte can be

comprehended by EIS. The Nyquist plots after the 1<sup>st</sup>, 10<sup>th</sup>, and 20<sup>th</sup> charge cycle of LFNO || graphite LIB cells assembled with the respective electrolytes at 20 °C are depicted in Figure 9. The impedance spectra were fitted to the equivalent circuit shown in Figure S5 to obtain the resistances/impedances throughout

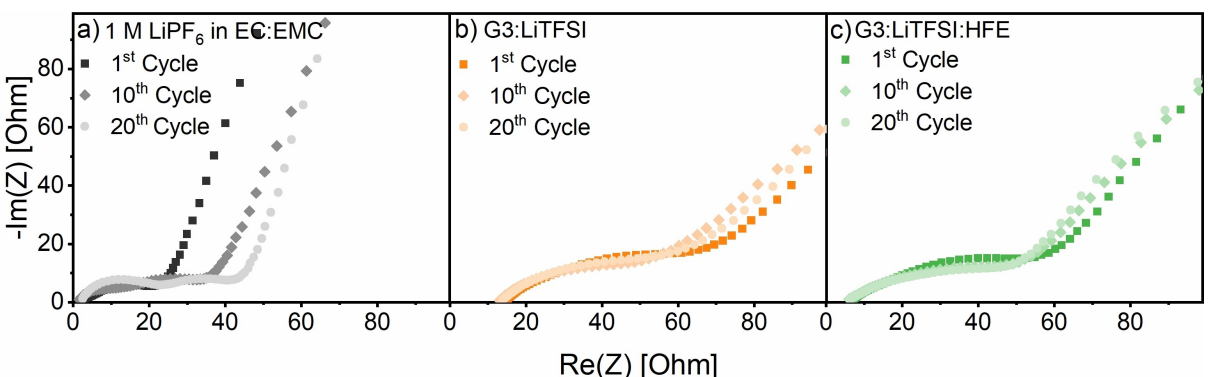


**Figure 9.** Nyquist plots of the electrochemical impedance measurements of the LFNO || graphite cells (LIB cell setup, control of cell voltage) at 100% SOC after the 1<sup>st</sup>, 10<sup>th</sup> and 20<sup>th</sup> cycle at 20 °C using a) the carbonate-based electrolyte, b) G3:LiTFSI and c) G3:LiTFSI:HFE. Cell voltage range: 0.5–4.6 V, charge/discharge current: 0.1 C (30 mA g<sup>-1</sup>).

cycling (Tables S1 and S2). The high frequency region of the spectra represents the Ohmic resistance of the cells, which comprises the ionic resistance of the respective electrolyte and additional minor Ohmic resistances of the current collectors and other cell components.<sup>[36]</sup> In agreement with the ionic conductivities of the investigated electrolytes (Figure S1), the highly viscous, undiluted SIL G3:LiTFSI displays the highest Ohmic resistance, while the reference electrolyte exhibits the lowest value. Upon cycling, the Ohmic resistance for all cells only changes slightly (see Table S1).

The mid-frequency region on the other hand drastically changes between the 1<sup>st</sup> and 20<sup>th</sup> cycle, at least for the cells using the carbonate-based electrolyte. This region of the impedance spectra comprises the resistance of Li<sup>+</sup> migration through the interphases at the anode and cathode, Li<sup>+</sup> desolvation, double layer penetration and charge transfer resistance at the electrodes.<sup>[37]</sup> While these “interfacial/interphasial resistances” (including contributions from/at the interfaces and interphases) remain almost constant throughout cycling in the SILs, the cells using the reference electrolyte display notably increasing impedances from the 1<sup>st</sup> to the 20<sup>th</sup> cycle (Table S2). A factor contributing to the deterioration of the interfacial/interphasial properties could be the previously reported formation of a cation-densified layer at the surface of the active material particles. As the oxidized oxygen species form unstable environments, the TM atoms migrate to unoccupied Li<sup>+</sup> sites, which causes high-energy barriers for Li<sup>+</sup> transport due to a Li/TM ratio below the percolation threshold needed for facile diffusion within the DRX material.<sup>[10,11,38]</sup>

However, as the interfacial/interphasial resistances only increase for cells that use the organic carbonate-based electrolyte and remain stable throughout cycling in the SILs, an electrolyte-based phenomenon, i.e., chemical or electrochemical electrolyte decomposition, seems more likely as the main root cause.<sup>[39]</sup> The electrochemical stability for the different electrolyte formulations was investigated by linear sweep voltammetry (Figure S6). The SILs exhibit a similar (G3:LiTFSI) or even reduced (G3:LiTFSI:HFE) oxidative stability compared to the reference electrolyte and show no deterioration of the interfacial/interphasial transport properties upon cycling. Therefore, a chemical rather than an electrochemical decomposition of the carbonate-based electrolyte seems to be responsible for the poorer cycling stability than with the SIL based cells. As proposed by Yabuuchi et al., anionic redox activity of the positive electrode upon delithiation releases oxygen species that are reduced to form superoxides. These superoxides are highly reactive towards organic carbonates and thus can decompose them chemically.<sup>[20]</sup> The solid reaction products that result from the decomposition of the carbonate-based reference electrolyte then accumulate at the electrode|electrolyte interfaces and thereby cause an ongoing growth or densification of the SEI and/or CEI layers.<sup>[40]</sup> Consequently, the transport properties at the respective electrode|electrolyte interfaces are deteriorated, which explains the steadily increasing overpotentials for the anionic and transition metal redox observed in the differential capacity vs. voltage plots of cells using the carbonate-based electrolyte as well as the growing

interfacial/interphasial resistances shown by EIS. However, electrochemical decomposition of the electrolyte as the cause for growing overpotentials could also play a role, since the electrochemical stability at a Pt electrode differs from the actual stability at a composite electrode due to the variation of the chemical environment and the electrodes' surface area.<sup>[41]</sup>

The reduced capacities and the continuous electrolyte decomposition found for LIB cells using the reference electrolyte also result in cathodic overcharge, as can be observed from the evolution of the LFNO end-of-charge (EOC) potential (measured by a three-electrode setup using Li metal as RE) in the different electrolytes throughout cycling (Figure 10). Note that the initial EOC potential for the electrodes differs due to varying initial discharge capacities in the electrolytes, which in comparison to the standard case results in deviations for the practical capacity balancing (N:P ratio) of the LIB cells.<sup>[42]</sup>

Nevertheless, clear differences can be observed for the evolution of the LFNO EOC potentials upon cycling. While the EOC potential of the LFNO electrode cycled in the reference electrolyte increases by almost 200 mV from the 1<sup>st</sup> to the 100<sup>th</sup> cycle, the EOC potential of the LFNO electrodes cycled in either SIL increases by less than 50 mV. Because the LIB cells are cycled by controlling the cell voltage, i.e., the potential difference between positive and negative electrode, the positive electrode EOC potential increases simultaneously with the EOC potential of the negative electrode.<sup>[43]</sup> As the local negative electrode potential is related to the degree of Li<sup>+</sup> intercalation into graphite, the rising EOC potential of LFNO observed for all electrolyte composition can be explained by the loss of active lithium, which generally occurs for DRX cathodes due to the partial irreversibility of anionic redox and the associated cation migration.<sup>[16,17]</sup> The more notable rise in LFNO EOC potential observed in the carbonate-based electrolyte can be explained by the lithium loss caused by electrolyte

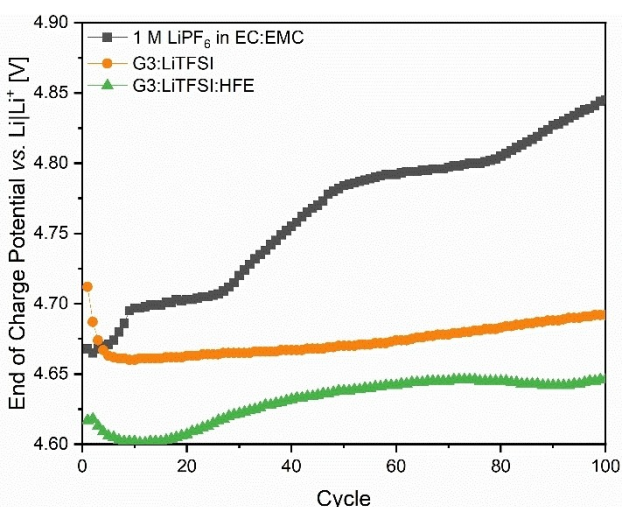


**Figure 10.** Evolution of the LFNO end-of-charge (EOC) potentials for the first 100 cycles of LFNO || graphite cells (LIB cell setup, control of cell voltage; three-electrode configuration with Li metal RE) at 20 °C assembled with the reference electrolyte, G3:LiTFSI and G3:LiTFSI:HFE. Cell voltage range: 0.5–4.6 V, charge/discharge current: 0.1 C (30 mA g<sup>-1</sup>).

decomposition, which further reduces the amount of Li<sup>+</sup> intercalated into graphite. Consequently, the EOC potential of the negative graphite electrode increases and the EOC potential for the positive electrode follows along. This rise of EOC potential is particularly detrimental for the positive electrode as cycling to a higher cut-off potential (often referred to as ‘cathode overcharge’) triggers aging mechanisms and structural instability of the active material.<sup>[44]</sup> Furthermore, the delithiation of LFNO at such high potentials is mainly accompanied by anion oxidation.<sup>[11]</sup> This increased utilization of the anionic redox activity results in an earlier depletion of the discharge capacity, as observed in the cycling data. Besides that, the rise in the local positive and negative electrode potentials also explains the deterioration of the TM redox, which was particularly pronounced in dQ/dV vs. voltage plots of LIB cells using the carbonate-based electrolyte. As the end-of-discharge (EODC) potential of the LFNO electrode also constantly increases throughout cycling in the reference electrolyte (Figure S7), the local potential of the LFNO electrode is not low enough to complete the reduction of (formerly oxidized) Fe<sup>3+</sup> species, which takes place at cell voltages below 2.6 V (i.e., at potentials below  $\approx$  2.8 V vs. Li|Li<sup>+</sup>) in the initial cycle (Figure 8a).<sup>[11]</sup> Thus, the TM-based capacity also decays because of undesired potential shifts throughout cycling in the carbonate-based electrolyte, which are a direct consequence of the increasing overpotentials and Li loss due to chemical electrolyte decomposition.

#### Post mortem analysis of LFNO positive electrodes

To confirm our hypothesis of severe chemical electrolyte decomposition for cells assembled with the carbonate-based electrolyte, LFNO electrodes cycled in the different electrolytes were investigated *post mortem* after 100 cycles by SEM and ATR-FTIR. While SEM images give insights on the surface morphology, ATR-FTIR can be utilized to identify functional groups of decomposition-species that accumulate on the surface of cycled LFNO electrodes in the respective electrolyte.<sup>[45–47]</sup>

ATR-FTIR spectra for a pristine LFNO electrode, LFNO electrodes cycled in the different electrolytes at 20 °C, and additional reference spectra of polyvinylidene difluoride (PVDF), lithium fluoride (LiF) and lithium carbonate (Li<sub>2</sub>CO<sub>3</sub>) for ease of comparison are depicted in Figure 11. The pristine LFNO electrode exhibits absorption bands at 1410, 1180 and 870 cm<sup>-1</sup>, which can be assigned to the PVDF binder. An absorption band at 1415 cm<sup>-1</sup>, originating from C–O asymmetric and symmetric stretching modes of Li<sub>2</sub>CO<sub>3</sub>, also indicates the presence of Li<sub>2</sub>CO<sub>3</sub> at the surface of the pristine LFNO electrodes. Similar to layered oxides, Li<sub>2</sub>CO<sub>3</sub> on the surface of pristine LFNO electrodes can be formed by a reaction between the active material and CO<sub>2</sub> from the air during processing.<sup>[48]</sup>

In comparison to the pristine electrode, the spectra of the cycled LFNO electrode in the carbonate-based electrolyte exhibits reduced intensities for the spectral features of PVDF and a novel peak at 835 cm<sup>-1</sup>, which can be assigned to the

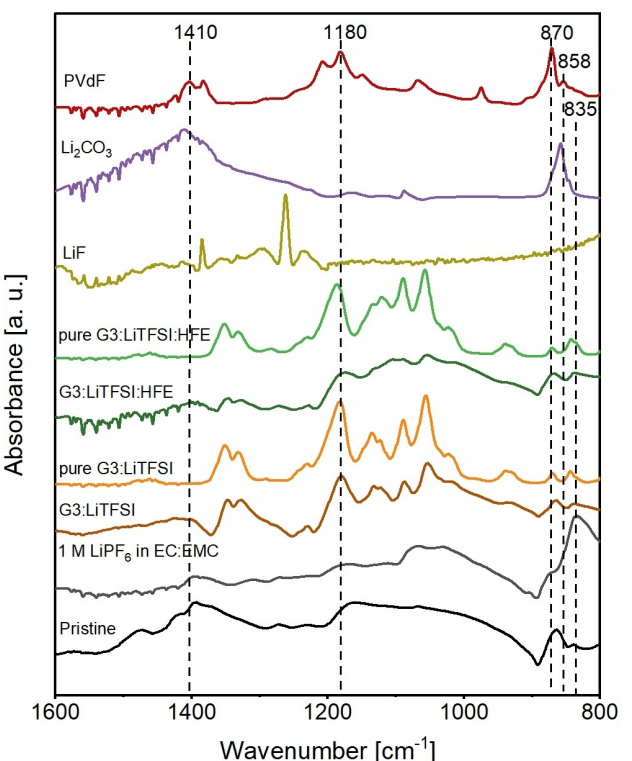


**Figure 11.** ATR-FTIR spectra of LFNO electrodes cycled for 100 cycles in a LIB cell setup using the reference electrolyte (black), G3:LiTFSI (dark orange) and G3:LiTFSI:HFE (dark green) at 20 °C. Additionally, reference spectra of pure lithium carbonate (Li<sub>2</sub>CO<sub>3</sub>; purple), the neat SILs (light orange and light green), PVDF (red), lithiumfluoride (LiF, yellow) and a pristine LFNO electrode ('pristine'; black) are shown.

P–F stretching mode from LiPF<sub>6</sub> or its decomposition products (i.e., halo-phosphides, Li<sub>x</sub>PF<sub>y</sub>O<sub>z</sub>).<sup>[45]</sup> Furthermore, a low-intensity spectral feature at 1310 cm<sup>-1</sup> can be assigned to LiF, which also exhibits absorption at this wavelength and is known to contribute to the interphase formation for LiPF<sub>6</sub> containing electrolytes.<sup>[46]</sup> Further electrolyte residues or decomposition products seem to be eliminated by the washing procedure prior to the ATR-FTIR measurements. Nevertheless, the occurrence of novel spectral features and reduced intensities for materials of the positive electrode give clear evidence for the formation of a passivation layer on top of the LFNO electrode cycled in the carbonate-based electrolyte.

The LFNO electrodes cycled in the diluted and undiluted SIL also display novel absorptions in the range from 1000–1450 cm<sup>-1</sup> compared to the pristine electrode. However, comparison of ATR-FTIR spectra of the neat SILs and the LFNO electrodes cycled in the SILs leads to the conclusion that these absorptions originate from residual SIL on the electrodes surface. As there are no significant differences observable between the spectral features of the neat SILs and their residues on the cycled LFNO electrodes, the decomposition of the SILs at the LFNO electrode can be ruled out. The detection of typical electrolyte decomposition products for LiPF<sub>6</sub>-based liquid electrolytes and the absence of decomposition products for both SILs are further supported by the surface morphology

of *post-mortem* LFNO electrodes, which was investigated via SEM (Figure 12).

While the surface of the electrodes cycled in the SILs (Figure 12c and d) resembles the surface of the pristine LFNO electrode (Figure 12a) and open pores are still visible, the LFNO electrode cycled in the carbonate-based electrolyte (Figure 12b) is covered by a thick surface film and LFNO particles are no longer visible. This layer on top of the LFNO electrode exhibits absorptions in the FTIR spectra that have been assigned to typical decomposition products of carbonate-based electrolytes and are most likely to cause the increasing interfacial/interphasial resistances observed via EIS throughout cycling.

## Conclusion

In this work, the impact of solvate ionic liquids (SILs) on the electrochemical performance of a lithium-rich disordered rock salt (DRX) cathode, i.e.,  $\text{Li}_{1.25}\text{Fe}_{0.5}\text{Nb}_{0.25}\text{O}_2$  (LFNO), was systematically investigated in LFNO || Li LMB cells and LFNO || graphite LIB cells at different operating temperatures (20, 40 and 60 °C) and compared to state-of-the-art carbonate-based electrolytes.

As observed by SEM and further identified via ATR-FTIR, LFNO || graphite LIB cells cycled in the carbonate-based electrolyte suffer from severe (chemical) electrolyte decomposition at the positive electrode during charge/discharge cycling. As no thick passivation layer is observed for the LFNO electrodes cycled in the electrochemically less stable SILs, the observed decomposition of the carbonate-based electrolyte can be reasoned with the reaction between  $\text{LiPF}_6$ /organic carbonates and the highly reactive oxygen species, which are released because of the partially irreversible anionic redox activity of the DRX material. The continuous accumulation of electrolyte decomposition products in interphases deteriorates the transport properties at the electrode|electrolyte interface, as shown by EIS. These ever-growing interfacial/interphasial resistances cause an extra overpotential for the redox processes of LFNO, which results in an early depletion of the anionic redox activity and diminishes the achievable capacities. Because less active lithium ions are transferred between the electrodes, the local positive electrode potential at the end-of-charge increases steadily, which further deteriorates the performance, as cathodic overcharge and hampered TM redox are induced. These mechanisms of capacity fade can be alleviated using a SIL electrolyte such as  $[\text{Li}(\text{G3})]\text{[TFSI]}$ . Cells

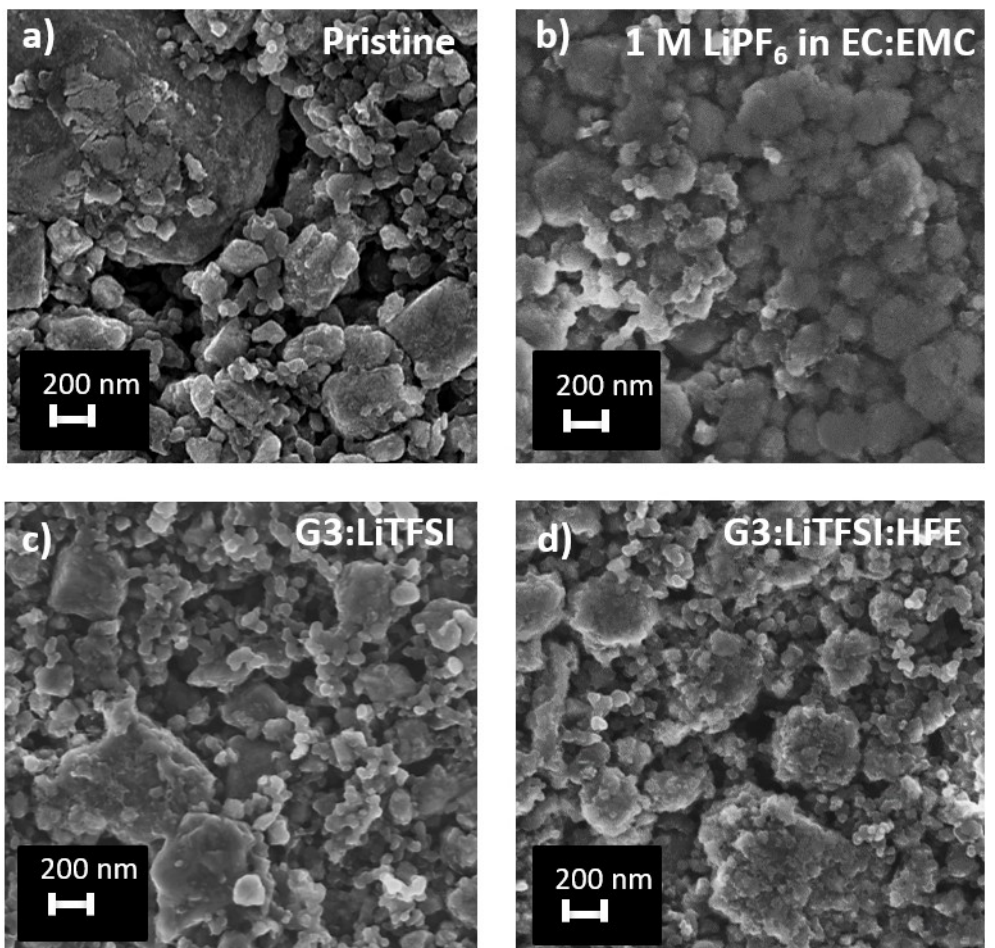


**Figure 12.** Representative SEM images of a pristine LFNO electrode and LFNO electrodes cycled in a LIB cell setup at 40 °C for 100 cycles in the different electrolytes. a) Pristine, b) cycled in the reference electrolyte, c) cycled in G3:LiTFSI and d) cycled in G3:LiTFSI:HFE.

assembled with the diluted and undiluted SIL electrolyte display a notable improvement in capacity retention compared to the reference system. Since the electrolyte is chemically stable towards the reactive oxygen species its decomposition can be avoided, which enables a stable electrode|electrolyte interface, less polarization, prolonged anionic redox activity and less cathodic overcharge. Nevertheless, further capacity decay mechanisms experienced for DRX cathodes, i.e., the formation of a cation-densified layer, detain a stable long-term performance of DRX-based LIB cells.

These results raise the question, whether DRX materials should still be evaluated in typical organic carbonate-based liquid electrolytes. Although DRX materials can be optimized to display less oxygen release in the future, which would reduce the improvements in capacity retention with SILs as the electrolyte, chemically more stable electrolytes should be included into studies to evaluate the cycling performance of DRX cathodes without interference of notable electrolyte decomposition.

## Experimental Section

### Electrode and electrolyte preparation

The DRX transition metal oxide with a composition of  $\text{Li}_{1.25}\text{Fe}_{0.5}\text{Nb}_{0.25}\text{O}_2$  was synthesized according to a procedure previously reported.<sup>[11]</sup> Composite electrodes with a composition of 80 wt.% carbon-coated LFNO, 10 wt.% carbon black as conductive agent (Super C65, Imerys Graphite & Carbon) and 10 wt.% PVDF (Solef 5130, Solvay) as a binder were prepared. *N*-methyl pyrrolidone (NMP; Aldrich) was used as processing solvent. For paste-preparation, LFNO particles were first mixed with carbon black for 15 min at a frequency of 15 s<sup>-1</sup> using a shaker mill with ZrO<sub>2</sub> balls (MM 400, Retsch GmbH). Afterwards, PVDF and NMP were added and the mixture was homogenized by shaker mill with a frequency of 20 s<sup>-1</sup> for 30 min and 30 s<sup>-1</sup> for 60 min. The paste viscosity was optimized to reach a solid content of 35 wt.%. The electrode paste was cast on Al foil (Evonik Industries) using a height adjustable doctor blade (Universal Applicator ZUA 2000.100 from Zehnter GmbH) with a wet film thickness of 100 µm. The electrode sheets were dried overnight at 80 °C in a drying cabinet. Circular electrodes with a diameter of Ø12 mm (for Swagelok®-type T-cell investigations; three-electrode configuration) and Ø14 mm (for coin-cell investigations; two-electrode configuration) were punched out from the sheets and dried overnight in a Glass Oven B-585 (Büchi Labortechnik AG) at 120 °C under reduced pressure ( $p < 0.05$  mbar). The active mass loading was  $\approx 3 \text{ mg cm}^{-2}$ , corresponding to an aerial capacity of  $\approx 0.9 \text{ mAh cm}^{-2}$  (considering 300 mAh g<sup>-1</sup> as the practical capacity (Q) of LFNO). Electrodes were densified using a hand press (Graseby Specac) applying 3.6 t cm<sup>-2</sup> for 15 s.

The composite graphite electrodes for LIB cell investigations contained 95 wt.% synthetic graphite SG3 (SGL Carbon), 4.5 wt.% sodium carboxymethyl cellulose as binder (NaCMC; Walocel CRT 2000, PPA 12, Dow Wolff Cellulosics) and 0.5 wt.% carbon black (Super C65, Imerys Graphite & Carbon) as a conductive agent. For electrode paste preparation, the Na-CMC binder was first dissolved in distilled water. Afterwards, graphite and carbon black were added. The mixture was homogenized using a high-energy mixer Dispermat® CV3-Plus (VMA-Getzmann GmbH) at 10,000 rpm for 1 h and at 500 rpm for 5 min. The viscosity was optimized to reach a

solid content of 40 wt.%. The electrode paste was then cast on smooth copper foil (Nippon Foil) using a height adjustable blade (Universal Applicator ZUA 2000.100 from Zehnter GmbH) with a wet film thickness of 150 µm. The electrode sheets were dried overnight at 60 °C in a drying cabinet. Circular electrodes with a diameter of Ø12 mm (for Swagelok®-type T-cell investigations) and Ø15 mm (for coin-cell investigations) were punched out from the sheet, and dried overnight in a Glass Oven B-585 (Büchi Labortechnik AG) at 80 °C under reduced pressure ( $p < 0.05$  mbar). The electrodes active mass was determined as  $\approx 2.5 \text{ mg cm}^{-2}$ , which results in an areal capacity of  $\approx 0.9 \text{ mAh cm}^{-2}$  ( $Q_{\text{Graphite}} = 360 \text{ mAh g}^{-1}$ ). The anodes were calandered to reach a porosity of 35%.

1.0 M LiPF<sub>6</sub> in EC:EMC (BASF SE, 3:7 by wt.%; purity: battery grade) was used as baseline carbonate-based electrolyte (referred to as the reference electrolyte throughout the text) and was used without further purification. For the preparation of the SIL electrolytes, triethyleneglycoldimethyleneether (G3; Sigma Aldrich; purity: > 98%) was purified via vacuum distillation over sodium and benzophenone. The H<sub>2</sub>O content was determined as  $\leq 40$  ppm by Karl-Fischer titration. 1,1,2,2-tetrafluoroethyl-2,2,3,3-tetrafluoropropyl ether (HFE; Synquest Labs; purity: > 99%) was purified via distillation. Lithium bis(trifluoromethanesulfonyl)imide (LiTFSI; BASF SE; purity: battery grade) was dried in a glass oven B-585 (Büchi Labortechnik AG) at 150 °C under reduced pressure ( $p < 0.05$  mbar) for two days. The SILs were synthesized in an argon-filled glovebox (H<sub>2</sub>O  $\leq 0.1$  ppm, O<sub>2</sub>  $\leq 0.5$  ppm, MBRAUN). G3 and LiTFSI were mixed in an equimolar ratio and stirred overnight at 40 °C to form the ionic liquid electrolyte referred to as the undiluted SIL G3:LiTFSI. The diluted SIL (G3:LiTFSI:HFE) was synthesized by stirring G3, LiTFSI and HFE in a molar ratio of 1:1:4.46 overnight at 40 °C.

### Cell assembly

Electrochemical investigations were performed in lab-scale Swagelok®-type T-cells (custom in-house design) in a three-electrode configuration and CR2032-type coin cells (316 L-grade stainless steel, TOB New Energy) in a two-electrode configuration. For coin cell testing, Ø15 mm circular negative (graphite or Li metal) and Ø14 mm circular positive electrodes (LFNO) were separated using a Ø16 mm polypropylene (PP) microporous monolayer membrane separator (Celgard 2500). The separator was wetted using 40 µL of the respective electrolyte. This two-electrode setup was used for constant current charge/discharge long-term cycling, C-rate and EIS investigations.

Swagelok® cells were assembled using Ø12 mm electrodes separated by a Ø13 mm PP fiber-based separator (Freudenberg, FS2190, 3 layers). A Ø6 mm Li metal foil (Albemarle Corporation; purity: battery grade) was used as reference electrode (RE) to monitor the evolution of individual electrode potentials of both positive and negative electrodes during long-term constant current charge/discharge cycling. A Ø10 mm PP fiber-based separator (Freudenberg, FS2190, 3 layers) was used to separate the counter (CE) and working electrode (WE) from the Li metal RE. 140 µL of the respective electrolyte was used for the Ø13 mm and 70 µL for the Ø10 mm separators, respectively. Swagelok® cells were used for cyclic voltammetry (CV) and chronocoulometry measurements. The balancing of the LFNO || graphite LIB cells, that is the ratio of the negative and positive electrode capacity, was based on the theoretical areal capacities of the electrodes (0.9 mAh cm<sup>-2</sup>, considering  $Q_{\text{LFNO}} = 300 \text{ mAh g}^{-1}$ ;  $Q_{\text{Graphite}} = 360 \text{ mAh g}^{-1}$ ). A negative to positive electrode capacity ratio (N:P ratio) of 1.00 was determined as optimal, since it resulted in sufficiently low negative electrode potentials to avoid overcharge of the positive electrode, while avoiding Li metal plating at the negative electrode.

## Electrochemical characterization

The electrochemical charge-discharge cycling performance of LFNO || Li LMB cells and LFNO || graphite cells (LIB cell setup; control of cell voltage<sup>[43]</sup>) was studied via constant current charge-discharge cycling on a MacCor 4000 battery testing system within climatic chambers set to 20, 40 or 60 °C. The LMB cells were operated in a voltage range from 1.5–4.6 V, while LIB cells were cycled in the cell voltage range from 0.5–4.6 V. The charge/discharge current was 0.1 C (30 mA g<sup>-1</sup>) for 100 cycles. At 60 °C the upper cut-off voltage was lowered to 4.5 V to avoid severe electrolyte decomposition. At least three cells per type of electrolyte and temperature were assembled to ensure a high reproducibility. The associated standard deviation is represented as error bars in the corresponding figures.

Constant current cycling at different specific currents (C-rate study) was carried out in LFNO || graphite LIB cells within a voltage range of 0.5–4.6 V. Charge and discharge C-rates of 0.1 C, 0.2 C, 0.5 C, 1 C and 2 C were each investigated for five cycles with no rest step in between. After five cycles at the highest C-rate of 2 C, the capacity retention at 0.1 C was investigated for five cycles.

Chronocoulometry and CV measurements were performed to determine the Al current collector dissolution behaviour of the electrolytes.<sup>[28]</sup> For that, Al foil was punched in Ø12 mm discs (Evonik Industries). The native passivation layer of Al was removed by submerging the foil into an aqueous solution of 5 wt.% KOH at 40 °C. The freshly etched electrodes were rinsed with de-ionized water and ethanol and dried under vacuum at 120 °C. The electrodes were transferred to a glovebox ( $H_2O \leq 0.1$  ppm,  $O_2 \leq 0.5$  ppm, MBRAUN) and used as the WE in three-electrode Swagelok® cells. Li metal was used as CE and RE. Chronocoulometry and CV measurements were carried out on a Versatile Multichannel Potentiostat (VMP; Bio-logic Science Instruments). A constant temperature was ensured by a climate chamber. For chronocoulometry measurements, the temperature was set to 20 °C and the cells were rested at open circuit potential (OCP) for 12 h. The WE potential was raised to 5 V vs. Li|Li<sup>+</sup> and held for 48 h while measuring the current. CV measurements were carried out at 20 °C in a potential range from 2.5 to 6.0 V vs. Li|Li<sup>+</sup>, using a scan rate of 1 mV s<sup>-1</sup>.

Electrochemical impedance spectroscopy (EIS) measurements were carried out on a VMP potentiostat using CR2032-type coin cells in a LIB cell configuration at 20 °C. After a 12 h OCV step, the cells were charged for 25 cycles according to the constant current charge/discharge protocol described above. EIS measurements were carried out at 100% state-of-charge (SOC) in each cycle. EIS was measured in a frequency range from 0.1 Hz to 0.1 MHz and a voltage amplitude of 10 mV.

## Characterization techniques

The 851 Titrando Karl Fischer Coulometer (Metrohm, Herisau, Switzerland) was calibrated with a threefold measurement of a 100 mg L<sup>-1</sup> water standard for quantification. Electrolytes were measured three times with an injection of 1 g, respectively. Instrument control, data acquisition and data evaluation were performed by Tiamo™ 2.4 (Metrohm) software.<sup>[49]</sup>

Cycled LFNO electrodes (after 100 cycles) were characterized by attenuated total reflectance Fourier-transformed infrared spectroscopy (ATR-FTIR) and scanning electron microscopy (SEM). Prior to the measurements, the cycled LFNO || graphite LIB cells were disassembled in the discharged state in an argon-filled glovebox ( $H_2O \leq 0.1$  ppm,  $O_2 \leq 0.5$  ppm). The LFNO electrodes were then rinsed using 200 µL EMC (battery grade, BASF) prior to surface

analysis, to remove electrolyte residues and LiPF<sub>6</sub> salt. ATR-FTIR measurements were performed on a Vertex 70 spectrometer (Bruker Optics) equipped with a Golden Gate ATR unit (Specac) using a KBr beam splitter. 256 measurements with a resolution of 2 cm<sup>-1</sup> in a frequency range from 500 to 4,000 cm<sup>-1</sup> were averaged. The sample chamber was continuously purged with a N<sub>2</sub>/Ar flow to minimize the influence of ambient conditions.

Linear sweep voltammetry (LSV) was carried out on a VMP potentiostat at 20 °C using three-electrode Swagelok® cells. A platinum electrode (Ø = 1 mm) was used as the working electrode (WE), Li metal as the counter and reference electrode. The cells were rested for 12 h at OCV. Then the current was measured while increasing the voltage from 3 to 6 V vs. Li|Li<sup>+</sup> with a scan rate of 0.1 mV s<sup>-1</sup>. SEM investigations were carried out by a Zeiss Auriga Electron Microscope (Carl Zeiss Microscopy GmbH) with a Schottky field emitter as electron source. Using the InLens detector, the typical working distance was 4 mm with an accelerating voltage of 3 kV. Prior to measurements, electrodes were dried under reduced pressure and transferred to the SEM in a vacuum-sealed sample holder to avoid exposure to air.

## Acknowledgements

We thank Adrian Fries for conducting the ionic conductivity measurements. We also thank Andre Bar for graphical support. Open Access funding enabled and organized by Projekt DEAL.

## Conflict of Interest

The authors declare no conflict of interest.

## Data Availability Statement

The data that support the findings of this study are available on request from the corresponding author. The data are not publicly available due to privacy or ethical restrictions.

**Keywords:** anionic redox · disordered rock salt (DRX) cathodes · electrolyte decomposition · lithium-ion batteries · solvate ionic liquids

- [1] a) T. Placke, R. Kloepsch, S. Dühnen, M. Winter, *J. Solid State Electrochem.* **2017**, *21*, 1939–1964; b) B. Dunn, H. Kamath, J.-M. Tarascon, *Science* **2011**, *334*, 928–935; c) M. Armand, P. Axmann, D. Bresser, M. Copley, K. Edström, C. Ekberg, D. Guyomard, B. Lestriez, P. Novák, M. Petranikova, W. Porcher, S. Trabesinger, M. Wohlfahrt-Mehrens, H. Zhang, *J. Power Sources* **2020**, *479*, 228708.
- [2] S. Dühnen, J. Betz, M. Kolek, R. Schmuck, M. Winter, T. Placke, *Small Methods* **2020**, *4*, 2000039.
- [3] F. Duffner, N. Kronemeyer, J. Tübke, J. Leker, M. Winter, R. Schmuck, *Nat. Energy* **2021**, *6*, 123–134.
- [4] J. B. Goodenough, K.-S. Park, *J. Am. Chem. Soc.* **2013**, *135*, 1167–1176.
- [5] a) J. U. Choi, N. Voronina, Y.-K. Sun, S.-T. Myung, *Adv. Energy Mater.* **2020**, *10*, 2002027; b) W. Li, E. M. Erickson, A. Manthiram, *Nat. Energy* **2020**, *5*, 26–34; c) Y. Arinicheva, M. Wolff, S. Lobe, C. Dellen, D. Fattakhova-Rohlfing, O. Guillou, D. Boehm, F. Zoller, R. Schmuck, J. Li, M. Winter, E. Adamczyk, Pralong V (Ed.) *Series on Advanced Ceramic Materials*, Elsevier, 2020.
- [6] M. Winter, B. Barnett, K. Xu, *Chem. Rev.* **2018**, *118*, 11433–11456.

- [7] a) J. B. Goodenough, *J. Power Sources* **2007**, *174*, 996–1000; b) M. S. Whittingham, *Chem. Rev.* **2004**, *104*, 4271–4301; c) R. J. Clément, Z. Lun, G. Ceder, *Energy Environ. Sci.* **2020**, *13*, 345–373.
- [8] R. Chen, S. Ren, X. Mu, E. Maawad, S. Zander, R. Hempelmann, H. Hahn, *ChemElectroChem* **2016**, *3*, 892–895.
- [9] N. Yabuuchi, M. Takeuchi, M. Nakayama, H. Shiiba, M. Ogawa, K. Nakayama, T. Ohta, D. Endo, T. Ozaki, T. Inamasu, K. Sato, S. Komaba, *Proc. Natl. Acad. Sci. USA* **2015**, *112*, 7650–7655.
- [10] R. Wang, X. Li, L. Liu, J. Lee, D.-H. Seo, S.-H. Bo, A. Urban, G. Ceder, *Electrochem. Commun.* **2015**, *60*, 70–73.
- [11] M. Luo, S. Zheng, J. Wu, K. Zhou, W. Zuo, M. Feng, H. He, R. Liu, J. Zhu, G. Zhao, S. Chen, W. Yang, Z. Peng, Q. Wu, Y. Yang, *J. Mater. Chem. A* **2020**, *8*, 5115–5127.
- [12] J.-P. Brinkmann, N. Ehteshami-Flammer, M. Luo, M. Leißing, S. Röser, S. Nowak, Y. Yang, M. Winter, J. Li, *ACS Appl. Energ. Mater.* **2021**, *4*, 10909–10920.
- [13] J. Lee, A. Urban, X. Li, D. Su, G. Hautier, G. Ceder, *Science* **2014**, *343*, 519–522.
- [14] D.-H. Seo, J. Lee, A. Urban, R. Malik, S. Kang, G. Ceder, *Nat. Chem.* **2016**, *8*, 692–697.
- [15] a) J. Lee, J. K. Papp, R. J. Clément, S. Sallis, D.-H. Kwon, T. Shi, W. Yang, B. D. McCloskey, G. Ceder, *Nat. Commun.* **2017**, *8*, 981; b) A. R. Armstrong, M. Holzapfel, P. Novák, C. S. Johnson, S.-H. Kang, M. M. Thackeray, P. G. Bruce, *J. Am. Chem. Soc.* **2006**, *128*, 8694–8698.
- [16] J. Lee, D.-H. Seo, M. Balasubramanian, N. Twu, X. Li, G. Ceder, *Energy Environ. Sci.* **2015**, *8*, 3255–3265.
- [17] D. Chen, W. H. Kan, G. Chen, *Adv. Energy Mater.* **2019**, *9*, 1901255.
- [18] G. Assat, J.-M. Tarascon, *Nat. Energy* **2018**, *3*, 373–386.
- [19] a) J. Lee, D. A. Kitchev, D.-H. Kwon, C.-W. Lee, J. K. Papp, Y.-S. Liu, Z. Lun, R. J. Clément, T. Shi, B. D. McCloskey, J. Guo, M. Balasubramanian, G. Ceder, *Nature* **2018**, *556*, 185–190; b) Y. Yue, N. Li, Y. Ha, M. J. Crafton, B. D. McCloskey, W. Yang, W. Tong, *Adv. Funct. Mater.* **2021**, *31*, 2008696.
- [20] N. Yabuuchi, K. Yoshii, S.-T. Myung, I. Nakai, S. Komaba, *J. Am. Chem. Soc.* **2011**, *133*, 4404–4419.
- [21] J. Li, S. Jeong, R. Kloepsch, M. Winter, S. Passerini, *J. Power Sources* **2013**, *239*, 490–495.
- [22] a) J. Herranz, A. Garsuch, H. A. Gasteiger, *J. Phys. Chem. C* **2012**, *116*, 19084–19094; b) G. A. Elia, J. Hassoun, W.-J. Kwak, Y.-K. Sun, B. Scrosati, F. Mueller, D. Bresser, S. Passerini, P. Oberhumer, N. Tsiovaras, J. Reiter, *Nano Lett.* **2014**, *14*, 6572–6577; c) T. Kuboki, T. Okuyama, T. Ohsaki, N. Takami, *J. Power Sources* **2005**, *146*, 766–769.
- [23] a) V. Baranchugov, E. Markevich, G. Salitra, D. Aurbach, G. Semrau, M. A. Schmidt, *J. Electrochem. Soc.* **2008**, *155*, A217; b) A. Guerfi, S. Duchesne, Y. Kobayashi, A. Vijh, K. Zaghib, *J. Power Sources* **2008**, *175*, 866–873.
- [24] K. Ueno, J. Murai, H. Moon, K. Dokko, M. Watanabe, *J. Electrochem. Soc.* **2017**, *164*, A6088–A6094.
- [25] H. Moon, T. Mandai, R. Tatara, K. Ueno, A. Yamazaki, K. Yoshida, S. Seki, K. Dokko, M. Watanabe, *J. Phys. Chem. C* **2015**, *119*, 3957–3970.
- [26] K. Ueno, J. Murai, K. Ikeda, S. Tsuzuki, M. Tsuchiya, R. Tatara, T. Mandai, Y. Umebayashi, K. Dokko, M. Watanabe, *J. Phys. Chem. C* **2016**, *120*, 15792–15802.
- [27] H.-M. Kwon, M. L. Thomas, R. Tatara, Y. Oda, Y. Kobayashi, A. Nakanishi, K. Ueno, K. Dokko, M. Watanabe, *ACS Appl. Energ. Mater.* **2017**, *9*, 6014–6021.
- [28] P. Meister, X. Qi, R. Kloepsch, E. Krämer, B. Streipert, M. Winter, T. Placke, *ChemSusChem* **2017**, *10*, 804–814.
- [29] E. Kramer, S. Passerini, M. Winter, *ECS Electrochem. Lett.* **2012**, *1*, C9–C11.
- [30] I. Cekic-Laskovic, N. von Aspern, L. Imholt, S. Kaymaksiz, K. Oldiges, B. R. Rad, M. Winter, *Top. Curr. Chem.* **2017**, *375*, 37.
- [31] K. Oldiges, N. von Aspern, I. Cekic-Laskovic, M. Winter, G. Brunklaus, *J. Electrochem. Soc.* **2018**, *165*, A3773–A3781.
- [32] Y. Yamada, C. H. Chiang, K. Sodeyama, J. Wang, Y. Tateyama, A. Yamada, *ChemElectroChem* **2015**, *2*, 1687–1694.
- [33] F. Holtstiege, A. Wilken, M. Winter, T. Placke, *Phys. Chem. Chem. Phys.* **2017**, *19*, 25905–25918.
- [34] a) J. Kasnatscheew, M. Evertz, B. Streipert, R. Wagner, R. Klöpsch, B. Vortmann, H. Hahn, S. Nowak, M. Amereller, A.-C. Gentsch, P. Lamp, M. Winter, *Phys. Chem. Chem. Phys.* **2016**, *18*, 3956–3965; b) N. Tran, L. Croguennec, M. Ménétrier, F. Weill, P. Biensan, C. Jordy, C. Delmas, *Chem. Mater.* **2008**, *20*, 4815–4825.
- [35] H. Ji, A. Urban, D. A. Kitchev, D.-H. Kwon, N. Artrith, C. Ophus, W. Huang, Z. Cai, T. Shi, J. C. Kim, H. Kim, G. Ceder, *Nat. Commun.* **2019**, *10*, 592.
- [36] J. Zhu, Z. Sun, X. Wei, H. Dai, *J. Appl. Electrochem.* **2016**, *46*, 157–167.
- [37] D. Andre, M. Meiler, K. Steiner, C. Wimmer, T. Soczka-Guth, D. U. Sauer, *J. Power Sources* **2011**, *196*, 5334–5341.
- [38] R. A. House, G. J. Rees, M. A. Pérez-Osorio, J.-J. Marie, E. Boivin, A. W. Robertson, A. Nag, M. Garcia-Fernandez, K.-J. Zhou, P. G. Bruce, *Nat. Energy* **2020**, *5*, 777–785.
- [39] R. Jung, M. Metzger, F. Maglia, C. Stinner, H. A. Gasteiger, *J. Phys. Chem. Lett.* **2017**, *8*, 4820–4825.
- [40] a) M. Winter, *Z. Phys. Chem.* **2009**, *223*, 1395–1406; b) D. R. Gallus, R. Wagner, S. Wiemers-Meyer, M. Winter, I. Cekic-Laskovic, *Electrochim. Acta* **2015**, *184*, 410–416.
- [41] J. Kasnatscheew, B. Streipert, S. Röser, R. Wagner, I. Cekic Laskovic, M. Winter, *Phys. Chem. Chem. Phys.* **2017**, *19*, 16078–16086.
- [42] J. Kasnatscheew, T. Placke, B. Streipert, S. Rothermel, R. Wagner, P. Meister, I. C. Laskovic, M. Winter, *J. Electrochem. Soc.* **2017**, *164*, A2479–A2486.
- [43] R. Nölle, K. Beltrop, F. Holtstiege, J. Kasnatscheew, T. Placke, M. Winter, *Mater. Today* **2020**, *32*, 131–146.
- [44] T. Ohsaki, T. Kishi, T. Kuboki, N. Takami, N. Shimura, Y. Sato, M. Sekino, A. Satoh, *J. Power Sources* **2005**, *146*, 97–100.
- [45] M. Kerlau, M. Marcinek, V. Srinivasan, R. M. Kostecki, *Electrochim. Acta* **2007**, *53*, 1385–1392.
- [46] K.-T. Kim, D. Kam, C. C. Nguyen, S.-W. Song, R. Kostecki, *Bull. Korean Chem. Soc.* **2011**, *32*, 2571–2576.
- [47] B. J. Tremolet de Villers, S.-M. Bak, J. Yang, S.-D. Han, *Batteries & Supercaps* **2021**, *4*, 778–784.
- [48] a) K. Matsumoto, R. Kuzuo, K. Takeya, A. Yamanaka, *J. Power Sources* **1999**, *81*–*82*, 558–561; b) N. Mijung, Y. Lee, J. Cho, *J. Electrochem. Soc.* **2006**, *153*, A935.
- [49] J. Henschel, F. Horsthemke, Y. P. Stenzel, M. Evertz, S. Girod, C. Lürenbaum, K. Kösters, S. Wiemers-Meyer, M. Winter, S. Nowak, *J. Power Sources* **2020**, *447*, 227370.

Manuscript received: February 10, 2022

Revised manuscript received: April 6, 2022

Accepted manuscript online: April 8, 2022